

See discussions, stats, and author profiles for this publication at: <https://www.researchgate.net/publication/236857821>

Stability and Relaxation Mechanisms of Citric Acid Coated Magnetite Nanoparticles for Magnetic Hyperthermia

DATASET *in* THE JOURNAL OF PHYSICAL CHEMISTRY C · FEBRUARY 2013

Impact Factor: 4.77 · DOI: 10.1021/jp311556b

CITATIONS

19

READS

243

10 AUTHORS, INCLUDING:



Marcela B. Fernández van Raap

National University of La Plata

60 PUBLICATIONS 287 CITATIONS

SEE PROFILE



Gustavo Pasquevich

National University of La Plata

30 PUBLICATIONS 159 CITATIONS

SEE PROFILE



Diego Muraca

University of Campinas

37 PUBLICATIONS 168 CITATIONS

SEE PROFILE



Francisco H Sánchez

National University of La Plata

182 PUBLICATIONS 1,225 CITATIONS

SEE PROFILE

Stability and Relaxation Mechanisms of Citric Acid Coated Magnetite Nanoparticles for Magnetic Hyperthermia

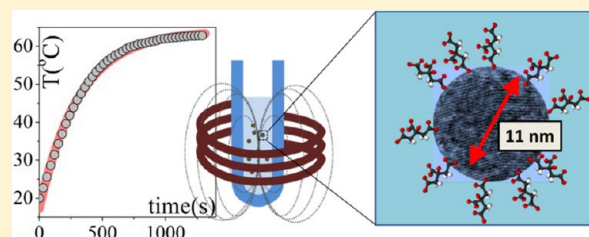
M. Elisa de Sousa,[†] Marcela B. Fernández van Raap,^{*,†} Patricia C. Rivas,[†] Pedro Mendoza Zélis,[†] Pablo Girardin,[†] Gustavo A. Pasquevich,[†] Jose L. Alessandrini,[†] Diego Muraca,[‡] and Francisco H. Sánchez[†]

[†]Instituto de Física de La Plata (IFLP- CONICET), Departamento de Física, Facultad de Ciencias Exactas, Universidad Nacional de La Plata (UNLP), c.c. 67, 1900 La Plata, Argentina

[‡]Instituto de Física "Gleb Wataghin" (IFGW), Universidade Estadual de Campinas, Brazil

S Supporting Information

ABSTRACT: Magnetite (Fe_3O_4) nanoparticles are proper materials for Magnetic Fluid Hyperthermia applications whenever these conjugate stability at physiological (neutral pH) medium and high specific dissipation power. Here, magnetite nanoparticles 9–12 nm in size, electrostatically stabilized by citric acid coating, with hydrodynamic sizes in the range 17–30 nm, and well dispersed in aqueous solution were prepared using a chemical route. The influence of media acidity during the adsorption of citric acid (CA) on the suspension's long-term stability was systematically investigated. The highest content of nanoparticles in a stable suspension at neutral pH is obtained for coating performed at pH = 4.58, corresponding to the larger amount of CA molecules adsorbed by one carboxylate link. Specific absorption rates (SARs) of various magnetite colloids, determined calorimetrically at a radio frequency field of 265 kHz and field amplitude of 40.1 kA/m, are analyzed in terms of structural and magnetic colloid properties. Larger dipolar interactions lead to larger Néel relaxation times, in some cases larger than Brown relaxation times, which in the present case enhanced magnetic radio frequency heating. The improvement of suspension stability results in a decrease of SAR values, and this decrease is even large in comparison with uncoated magnetite nanoparticles. This fact is related to interactions between particles.



1. INTRODUCTION

Stable dispersion of magnetic nanoparticles (MNPs) has attracted much attention, in a first stage because of their rheological properties¹ that allow dynamic control by applied fields and more recently due to their widespread biomedical diagnostic and therapeutic applications^{2,3} such as visualization agents in magnetic resonance imaging,⁴ therapeutic carriers in drug delivery,^{5,6} heat intermediaries in cancer treatment therapies,^{7,8} and labelers for in vitro and in vivo separation experiments.⁹ The usefulness of the magnetic colloids for biomedical application depends on their biocompatibility, the stability of the magnetic nanoparticles in solution at neutral pHs, and the capability of MNP surfaces to become chemically functionalized.

Among many studied materials, Fe and its oxides are the unique FDA (US Food and Drug Administration) accepted ones. The amphoteric surface of Fe oxides facilitates their functionalization. Subsequently, many protocols have been developed for its preparation by either high-temperature decomposition of an organic iron precursor or low-temperature coprecipitation.¹⁰ The MNPs produced by high-temperature decomposition methodology display better structural and magnetic properties but also hydrophobicity, and further work on MNP surfaces for their stabilization in neutral

conditions is needed. Stability in suspension is a major requirement for any biomedical application that involves injection in a living human being and results from the interplay between attractive dipolar and van der Waals interactions and repulsive electrostatic and steric interactions.

Steric stabilization includes coating with nonionic surfactant molecules, polymers, and inorganic layers as silica or some noble metals.¹¹ Among the routes employed for obtaining the water-soluble functionalized iron oxide MNPs, the addition of small biocompatible organic molecules, such as amino acids,¹² peptides,¹³ citric acid,^{14–16} and cyclodextrin,¹⁷ presents the advantages of combining electrostatic and steric stabilization, assuring coating biocompatibility and providing functionality for biomolecule conjugation. Comparing polymeric stabilization with electrostatic one presents the advantage of reversibility from the aggregated state by dilution but usually involves the binding of a large macromolecule resulting in a coated MNP with a large overall size which strongly modifies its hydrodynamic behavior. So, a renewed interest has appeared in iron oxide nanoparticles synthesized by coprecipitation and

Received: November 23, 2012

Revised: February 22, 2013

Published: February 22, 2013



Table 1. Synthesis, Magnetic and Structural Characterization Parameters, and Specific Absorption Rate (SAR) under a Radiofrequency Field of 265 kHz and 40.1 kA/m of Magnetite Aqueous Colloids, Stable in Suspension under Moderate Magnetic Fields^a

	[X] (g/L)	pH _{ads} ± 0.01	pH _{sus} ± 0.01	M _s (Am ² /kg)	d _m (nm)	σ _{dm}	δ (nm)	d _{TEM} (nm)	d _H (nm)	T _{Bi} (K)	T _B (K)	SAR (W/g)
CS ₁	13.4	4.58	7.44	16.0	7.1	2.5	5.3	9.5 ± 1.6	18.3	81	28	14.4
CS ₂	10.7	4.91	7.34	9.7	7.0	2.4	7.5	8.2 ± 2.4	17.8	92	41	4.29
CS ₃	18.3	5.50	6.97	24.9	6.0	2.8	3.1	9.3 ± 1.7	26.6	166	13	28.0
CS ₄	13.1	6.25	7.22	26.0	7.1	3.4	3.4	11.9 ± 3.5	23.4	196	18	41.5
CS ₅	5.6	6.88	7.10	17.7	5.8	2.5	4.0	9.4 ± 2.0	30.2	132	16	12.1
CS ₆	7.4	7.08	7.22	11.5	6.7	2.4	6.4	10.9 ± 1.8	20.2	126	32	5.2

^aCS_i (i = 1–6) labeled colloids synthesized by one-step coprecipitation at 60 °C, followed by citric acid adsorption at pH_{ads} medium acidity and finally suspended at pH_{susp}. [X] stands for concentration as mass of magnetite per solution volume; typical error is ±0.2. Data derived from SQUID-DC magnetometry: M_s stands for specific saturation magnetization, d_m for magnetic core diameter, σ_{dm} for standard deviation, and δ for twice the magnetically frustrated layer thickness. d_{TEM} stands for nanoparticle diameter retrieved from TEM images, d_H for weight (averaged nanoparticle hydrodynamic diameter), T_{Bi} for blocking temperatures determined from ZFC curve maximum, T_B for blocking temperature for same size noninteracting nanoparticles, and SAR for Specific Absorption Rate at 40.1 kA/m and 265 kHz in Watts per gram of magnetite.

stabilized by functionalization of their surface using small molecules with large deprotonation ability like organic polyprotic acids, leading to electrosteric stabilization.

Citric acid (AH₃ with A = C₆H₅O₇) is a small molecule that has three carboxyl and one hydroxyl groups and is known to chemisorb to the iron oxide nanoparticle by forming a carboxylate group with the Fe–OH molecules present on the nanoparticle surface, leaving one or two carboxyl groups negatively charged that can be used for other purposes. A positively charged drug¹⁶ and/or a fluorescent molecule, like for instance rhodamine,¹⁸ can be bonded to them for applications in drug delivery or for in vitro labeling studies, respectively. As the AH₃ molecule is small the nanoparticles' hydrodynamic radii are not much enlarged, which is of importance in magnetic hyperthermia therapy applications. Differences evidenced in the rheological and microstructural properties of biocompatible citric acid coated magnetites prepared by different protocols based on the coprecipitation method have been recently discussed elsewhere.¹⁵

Magnetic Fluid Hyperthermia is a therapy to treat cancer tumors. Briefly, MNPs exposed to a radio frequency (rf) field absorb energy from the applied field and dissipate this energy through magnetic relaxation effects locally raising the tumor temperature above 43 °C and selectively killing tumor cells.⁷ The figure of merit of a given nanoparticle for this application is given by the specific absorption rate (SAR), which is defined as the heat power absorbed from the rf field per gram of magnetic material. Nowadays, active research is being executed on MNPs synthesis protocol to improve specific absorption rates to reduce the amount of material that has to be incorporated into a given tumor for its treatment and also to extend this kind of therapy to smaller tumors, which requires the attainment of larger SAR values. For single-domain MNPs, relaxation processes are of the Néel and Brown types. These processes correspond to the nanoparticle magnetic moment switching among its easy axis directions and the viscous friction due to the Brownian rotational diffusion of particles in the fluid, respectively. As both processes take place in parallel, the heating is driven by the one having the shorter characteristic time.¹⁹ From the stabilization ways previously outlined emerges the possibility of either using MNPs with large hydrodynamic sizes (polymeric like coating) possibly resulting in a Néel driven process or using MNPs covered with small organic molecules, as the ones studied here, which may dissipate through a Brown type process. The question of which of these mechanisms

optimizes the heating process is still an open question, whose answer requires more experimental research.

In this work, highly stable and biocompatible magnetic suspensions of citric acid coated Fe₃O₄ nanoparticles in water were produced as biomedical colloids suitable for energy dissipation under an external ac magnetic field in the rf range and appropriated for magnetic hyperthermia therapy. Moreover, the specific heating efficiency at a frequency of 265 kHz and field amplitudes of 20, 27.8, and 40.1 kA/m were determined and are discussed here in terms of the MNP structural and magnetic parameters. Optimum synthesis conditions for long-term suspension stability, as well as the performance of the obtained ferrofluids for rf heating, are determined for a wide range of experimental conditions. A detailed analysis of SAR measured values in terms of magnetic and structural colloid properties is addressed. Finally, the coated MNPs were efficiently internalized by human lung adenocarcinoma A549 cells, and its viability was analyzed by flow cytometry using Annexin V - Propidium Iodide (PI) markers.

2. EXPERIMENTAL DETAILS

Fe₃O₄ nanoparticles (core) were prepared by coprecipitation of ferric chloride and ferrous chloride in the presence of excess ammonia NH₄OH solution (AS) via a modified Massart method.^{20,21} The so obtained magnetite cores were negatively charged by CA adsorption over its surfaces. The coating was performed without leaving the wet route, to avoid nanoparticle surface passivation. Both steps, coprecipitation and CA adsorption, were carried out under a N₂ reflux, to ensure anaerobic conditions, with continuous and vigorous magnetic stirring to ensure reagent homogeneity, and at controlled constant temperature equal to 60 °C. The heating device was close loop controlled to ensure temperature homogeneity and reproducibility.

Briefly, 2.75 g of FeCl₃·4H₂O and 1.01 g of FeCl₂·6H₂O were dissolved in 50 mL of bidistilled water each, mixed in a three-neck flask, and heated to the reaction temperature. Then, 3 mL of AS (25% w/w) was added drop by drop and left to react for 30 min; after that, 75 mL of AS was added at a rate of 1 drop/s until the solution reached a pH of 10.5, high enough to prevent agglomeration due to surface charge. The isoelectric point (IEP) of magnetite is known²² to be in the pH range from 6 to 7 depending on the Fe²⁺ concentration and temperature. Then, the black precipitate was separated from the dispersion medium

by means of a permanent magnet, mixed with a CA aqueous solution (0.02 g/mL), and left to react at 60 °C during 90 min to obtain citric acid coated magnetite. To yield uncoated magnetite (u), the black precipitate was washed several times and resuspended in water at a pH close to neutral (7–7.4).

The pH at which CA was adsorbed to the MNP surface (pH_{ad}) was varied from 4.58 to 7.08. AS (0.25% w/w) was used to adjust the suspension pH to pH_{sus} close to 7. Then the suspension was again placed in a permanent magnet during 600 s. By this way six colloids C_i (with $i = 1$ to 6 for increasing pH_{ad}) were prepared. Each one of them was then divided into two parts: the suspension of MNPs that were immobilized with a permanent magnet (CP_i) and the suspension of the MNPs which remained suspended under the moderate magnetic field created by the magnet (CS_i). Details about the preparation of the six CS_i colloids of Fe_3O_4 nanoparticles coated at different pH_{ad} are given in Table 1. pH measurements were carried out with a pH-meter with ± 0.01 pH accuracy.

Common and standardized chemical volumetric analysis was used for colloid concentration $[x]$ determination, expressed as magnetite mass per solvent volume with an accuracy of 2%. $\text{K}_2\text{Cr}_2\text{O}_7$ was used as titrant.

Phase identification and core particle characterization were performed by X-ray diffraction (XRD) and transmission electron microscopy (TEM) on dried samples. Dried coating easily hydrates, hindering sample preparation for XRD analysis, especially in the more efficiently coated cases. The patterns were determined with an X'Pert Diffractometer within a 2θ range from 20 to 80°. TEM images were obtained with a TEM JEOL JEM 2100 microscope.

Zeta-potential measurements and thermogravimetry (TG) combined with differential thermal analysis (DTA) were used to confirm coating achievement. Measurements were carried out on dried powder samples with a Shimadzu TG-50 and DTA-50 system. During measurements the samples were kept inside platinum crucibles and heated at a constant rate of 10 K/min under a flux of 50 mL/min of N_2 . The laser doppler electrophoretic method was used to measure zeta potentials (ζ [mV]) of 1 mL of colloid with a Malvern Zetasizer nano ZS90 device. The zeta potential was obtained by the application of the Henry equation using the Hückel approximation.

Dynamic light scattering (DLS) experiments were performed on CS_i colloids at a scattering angle of 90 °C with a goniometer ALV/CGS-5022F with Multiple Tau digital correlator ALV-5000/EPP. The light source was a helium–neon laser operating at 22 nW.

Specific magnetization (M) as a function of applied magnetic field (H) at room temperature was obtained using a VSM LakeShore 7404 vibrating sample magnetometer operated with a maximum applied field $\mu_0 H_{\text{max}} = 1.5$ T or with a SQUID Quantum Design magnetometer with $\mu_0 H_{\text{max}} = 2.5$ T. The latter was also used to measure the magnetization temperature dependence under zero field cooled (ZFC) and field cooled (FC) protocols carried out at 2 K/min and $H_{\text{FC}} = 100$ Oe.

Hydrodynamic sizes were obtained from the inverse Laplace transformation of the measured time correlation function assuming the Stokes–Einstein relation between relaxation times and hydrodynamic diameters.²³ Each sample was measured 10 times. Mean values (d_{H}) of the weight-average hydrodynamic sizes are reported in Table 1.

Time-dependent calorimetric experiments were conducted exposing 1 mL of the colloid, held in a clear glass Dewar, to rf fields of 20, 27.8, and 40.1 kA/m amplitude and 265 kHz

frequency. The temperature was sensed during treatment with a fiber optic sensor placed at the center of the sample. The sensor was connected to a calibrated signal conditioner (Neoptix) with an accuracy of ± 0.1 °C. Colloid temperature was kept below 65 °C to minimize evaporation and prevent colloid destabilization.

The SAR parameter was obtained from the initial slope of the heating curve with the expression

$$\text{SAR} = \frac{C}{[X]} \frac{\partial T}{\partial t} \quad (1)$$

where C is the volumetric heat capacity of the solvent ($C = 4.18$ J/K cm³) and $[X]$ is the MNP concentration given as mass of Fe_3O_4 per solvent volume unit.

Viability and discrimination of apoptotic and necrotic cells were determined by double-labeling for the Annexin V and PI assay and analyzed by flow cytometry using a PARTEC PAS III cytometer. It is known²⁴ that the plasmatic membrane loses phospholipid asymmetry in the apoptosis, resulting in the exposure of phosphatidylserine (PS) residues at the outer plasma membrane leaflet. Annexin V interacts strongly and specifically with PS, and it is used to detect apoptosis by targeting for this asymmetry. Annexin V does not bind to normal live cells since the molecule is not able to penetrate the phospholipid bilayer. In necrotic cells the integrity of the plasma membrane is lost, and then Annexin V is able to bind to the cell. To discriminate between necrotic and apoptotic cells PI (a membrane-impermeable DNA stain) is simultaneously used.

A549 cells were grown as monolayer in Dulbecco's modified Eagle's medium (DMEM) supplemented with 10 vol % fetal bovine serum and 0.5 mg mL⁻¹ of streptomycin in a humidified 5% CO_2 atmosphere at 37 °C. For the MNP uptake, the cultures at 60% confluence (24 h incubation time) were washed with phosphate buffered saline (PBS) and were incubated, in 18 mL of DMEM doped with three distinct concentrations of 34, 67, and 135 $\mu\text{g}_{\text{Fe}_3\text{O}_4}/\text{mL}$ of culture medium, in a 75 cm² flask during 12 h. Then, cells were washed four times with PBS to remove the nonincorporated MNPs and trypsinized from each flask. From each A549 internalized culture, 10⁶ cells were resuspended in Annexin-binding buffer and stained with 5 μL of Annexin and 5 μL of propidium iodide. Cells incubated without nanoparticles at the same condition of the internalized ones (36 h incubation time) were used as control.

3. RESULTS AND DISCUSSIONS

3.1. Stability Analysis. The crucial step in the preparation of a stable aqueous suspension of MNPs resides on their surfaces engineering, in this case on the CA adsorption efficiency. Representative DTA-TG curves of citric acid and the CS_i colloid are shown in Figure 1a and b, respectively. The DTA curve in Figure 1(a) displays a sharp endothermic peak at 157 °C without weight loss at the corresponding TG, assigned to fusion ($\Delta H_{\text{fus}} = -0.14$ kJ/g), and a broad endothermic feature (centered at 217 °C), assigned to citric acid decomposition ($\Delta H = -0.55$ kJ/g), happening in many steps. TG data show an abrupt single-step weight loss (onset at 209 °C) of 87.5% due to CA decomposition. On the other hand, no fusion peak appears at the DTA curve (Figure 1b) of coated nanoparticles, indicating the absence of free CA precipitation, and exothermic peaks related to magnetite oxidation commencing around 200 °C are superimposed to attached CA decomposition. The TG curve displays a two-step

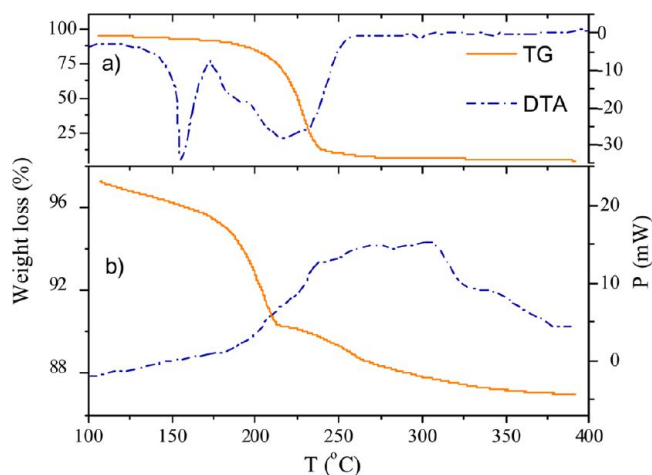


Figure 1. TG and DTA plots of neat citric acid at the upper part (a) and CS_i colloid at the lower part (b).

weight loss (onsets at 175 and 222 $^{\circ}\text{C}$) of 7.3 and 2.5% which is attributed to desorption of citric acid molecules from the nanoparticle surface.¹⁸ Two-step weight loss is an indication of a bilayer coating formation: at the first layer the CA molecules are chemically attached to the MNP surface and the second is bound to the first through hydrogen bonds. The latter desorbs at lower temperature. Two-step weight loss has been observed at the MNP coated by bilayers of *n*-alkanoic acids.²⁵ From the comparison of these thermogravimetric curves it is inferred that the binding of the CA molecule to the MNP surface was accomplished.

Both types of aqueous suspensions (CP_i and CS_i) are very stable, and the MNPs remain suspended for periods of several months, CS_i colloids being extremely stable. For CS_i colloids the separation of the MNPs from the dispersion media was not even possible by three times centrifugation at 13 000 rpm during 600 s. The mass fraction (f) of suspended nanoparticles, defined as the quotient of concentrations, measured at pH_{sus} , $f = [\text{CS}_i]/[\text{C}_i]$, was used as a parameter to quantify the CA adsorption efficiency and as a long-term stability criterion. In Figure 2, it can be seen that f decreases monotonically with pH_{ads} . The aqueous citric acid solution left to react with the oxide particles during the synthesis consists of a pH-dependent mixture of AH_3 , AH_2^- , AH^{2-} , and A^{3-} . The molar fractions x_y ($y = \text{AH}_3$, AH_2^- , AH^{2-} , and A^{3-}) calculated using the known acid dissociation constants $\text{pK}_{\text{a}1} = 3.13$, $\text{pK}_{\text{a}2} = 4.76$, and $\text{pK}_{\text{a}3} = 6.40$ are included in Figure 2. The larger f value is achieved for CA adsorption at $\text{pH}_{\text{ads}} = 4.58$, when 60% of CA molecules were negatively charged as AH_2^- and 40% as AH^{2-} . The decrease of AH_2^- and AH^{2-} occurring at pH larger than 5.5 disfavors stability. At pH values lower than 4.58, there is a large dissolution rate, and the MNP dissolves during preparation.²⁶

Zeta-potential (ζ) measurements of CS_2 , CS_4 , CS_6 , and u colloids are shown in Figure 3, and the mean ζ values against pH are displayed in Figure 4. The isoelectric point (IEP) of coated nanoparticles is close to 2, and for $\text{pH} > 4$ the largest mean value of ζ is close to -36 mV. Results suggest that at larger pH_{sus} stability occurs when a larger amount of AH_2^- is present at binding conditions; i.e., a larger amount of CA binds to the nanoparticle surfaces by one carboxylate leaving two free dangling ends. Further deprotonation of an already bonded molecule occurs at pH value larger than $\text{pK}_{\text{a}3} = 6.40$, providing electrostatic and steric stabilization. Mean ζ values as large as

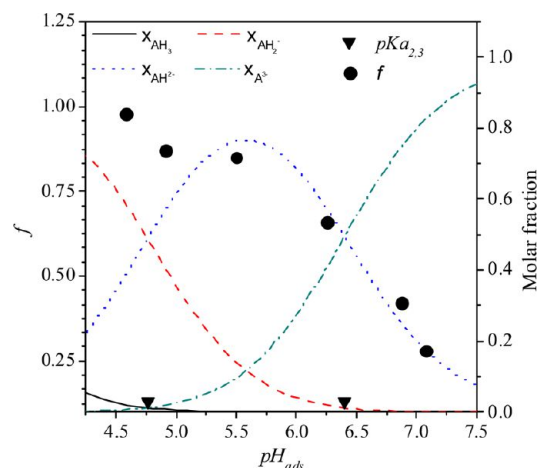


Figure 2. Dots stand for the fraction (f) of MNP that remains stable at neutral pH after exposure to 0.1 T during 600 s, used as a long-term stability parameter, triangles for acid dissociation constants (pK_{a}), and pH_{ads} for adsorption pH. Lines stand for theoretical calculations of molar fraction of the species composing the aqueous citric acid solution vs adsorption pH_{ads} using equilibrium dissociation constants for deprotonation reactions.

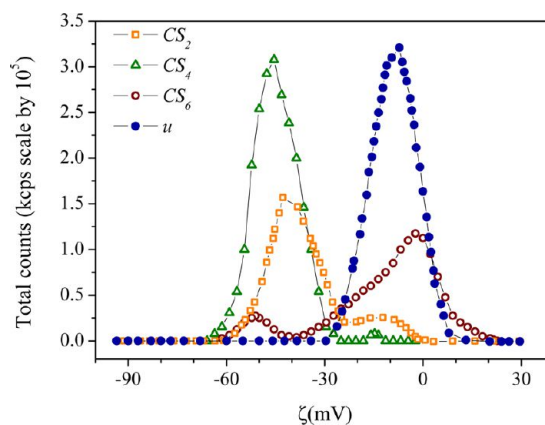


Figure 3. Zeta potential (ζ) distribution of coated MNPs measured at neutral suspension pH.

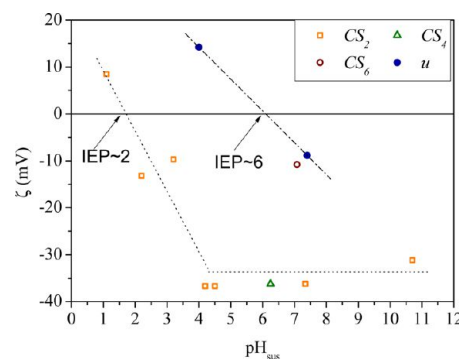


Figure 4. Mean zeta potential (ζ) against suspension pH_{sus} . Lines stand to guide the eye and IEP for the isoelectric point.

-36 mV confirm that the particles have become highly negatively charged and that the coating was accomplished. Our results differ from a previous work⁴ where the largest amount of magnetic nanoparticles in stable suspension at $\text{pH}_{\text{sus}} = 10.1$ was obtained with CA adsorption at 80 $^{\circ}\text{C}$ and $\text{pH}_{\text{ads}} = 5.2$ where 70% the molecules are twice deprotonated as AH^{2-}

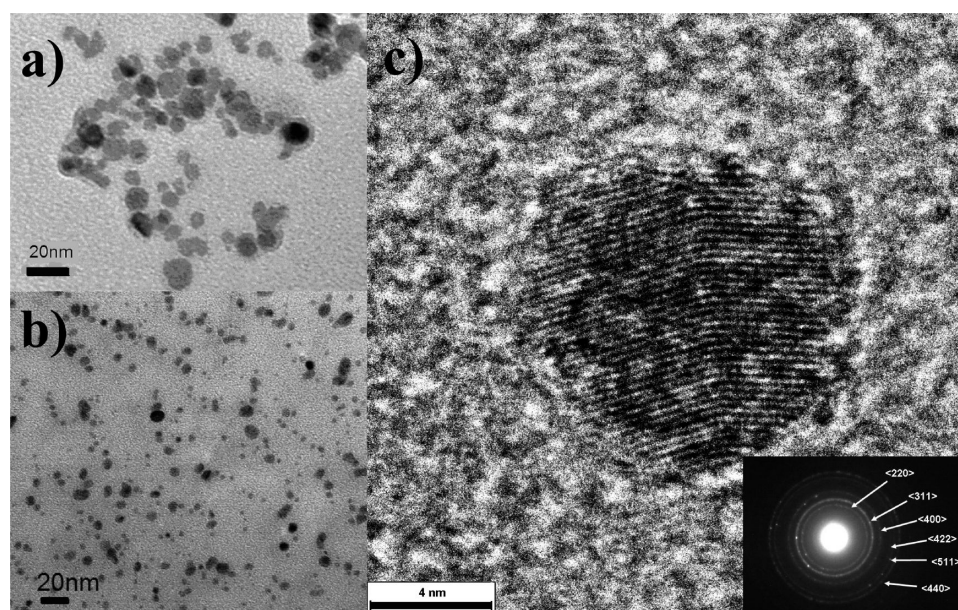


Figure 5. TEM images of uncoated (a) and citric acid coated particles (CS₆) (b) and isolated particle of CS₆ dried colloid (c).

and 25% once deprotonated; however, the largest $|\zeta|$ determined in both works coincide because both were measured at pH values larger than pK_{a3} where the three carboxyl groups are dissociated. A largest ζ value of -25.6 at pH 6 was obtained in other recent work¹⁶ where coated magnetite was optimized for drug delivery. A lower ζ value means less charge and may be related to a shorter adsorption time (30 min less).

3.2. Structural and Magnetic Analysis. X-ray diffractograms for u and CS_{*i*} samples present typical X-ray diffraction patterns of magnetite (see Figure S1 in Supporting Information). The diffraction patterns display well-defined peaks belonging to the cubic spinel structure, indicating that the samples are single phase. The whole patterns were refined, including peak broadening due to crystallite size, using a cubic spinel structure (space group Fd3m) with lattice parameter $a = 8.378$ Å and the O atoms arranged in a face-centered-cubic lattice. Figure 5a displays a typical TEM image of u -MNPs ($d_{\text{TEM}} = 9.9 \pm 2.4$ nm). These particles are not regularly faceted; instead they show spheroid-like forms and are quite aggregated. A representative TEM image of a coated colloid (CS₆) is shown Figure 5b and a single CS₆ particle in Figure 5c. The selected area electron diffraction pattern indicates good crystallinity (see inset of Figure 5c). The MNPs are spherical, more uniform, and further apart from each other than uncoated nanoparticles. Chain-like arrangements due to dipolar interactions appear. Mean size values estimated from TEM data are listed in Table 1. CS_{*i*} and CP_{*i*} colloids display similar mean size; for example, d_{TEM} for CP₆ is 10.8 ± 2.7 nm.

Magnetic analysis was performed on dried colloid samples and on frozen uncoated and both CS_{*i*} and CP_{*i*} coated colloids. Each sample is a collection of single domain particles of magnetic volume V and giant magnetic moment $\mu = M_p V$ (ρ is the mass density). Particle magnetocrystalline anisotropy axes are randomly distributed. The energy of this ensemble placed in a magnetic field H arises from three main contributions, the magnetic anisotropy energy, the particle magnetic moment Zeeman interaction with the applied field, and the dipolar interaction among particles.

The first and third energy terms dominate at low field, and then determine the magnetization behavior as a function of temperature in FC and ZFC curves displayed in Figure 6 for u

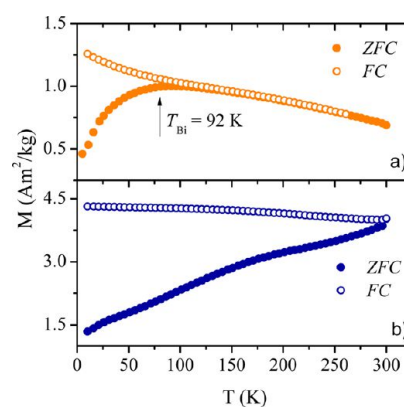


Figure 6. Specific magnetization temperature dependence for zero-field-cooled (ZFC) and field-cooled (FC) protocols for (a) CS₂ and (b) uncoated colloids (dried samples), acquired with $H_{\text{FC}} = 100$ Oe and heating rates of 2 K/min.

and CS₂ samples. The absence of a maximum in the ZFC curve of the u sample indicates a blocking temperature close to room temperature due to aggregation and strong dipolar interaction between particles. The constancy of M almost in the whole FC curve is also a signature of a highly interacting system. The ZFC curve of CS₂ exhibits a maximum at the blocking temperature $T_{\text{Bi}} = 92$ K, and ZFC bifurcates from the FC curve at the irreversibility temperature $T_i = 140$ K. For temperatures higher than T_i , magnetization temperature dependence strongly departs from the Curie-like behavior ($M \sim H/T$) expected for a noninteracting system. As temperature decreases from T_i , the FC magnetization increases. Comparing ZFC–FC curves of uncoated and coated MNPs it is clear that citric acid coating prevents strong aggregation and lowers dipolar interaction, but still the system behaves as an interacting superparamagnet

(ISP). Colloids blocking temperatures T_{Bi} obtained from ZFC data acquired from frozen colloids are listed in Table 1.

The second energy term dominates at high fields and is the main contribution to the hysteresis loops shown in Figure 7.

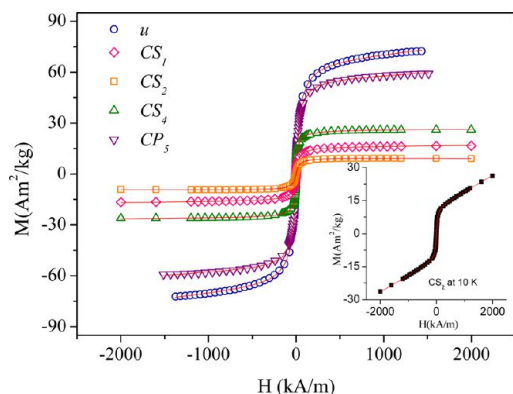


Figure 7. Specific magnetization loops measured at 290 K for various colloids. Inset: CS_2 measurement at 10 K. Solid lines stand for best Langevin fits using eq 2.

The mean particle magnetic moment $\langle\mu\rangle$ in all the studied samples is around $1.5 \times 10^4 \mu_B$; the anisotropy energy barrier $K_{eff}V$ is much smaller than the magnetic moment field interaction energy $\mu_0\mu H$; and the magnetization of the particles at a given temperature and field can be modeled as

$$M(T, H) = N \int_0^\infty \mu L\left(\frac{\mu_0\mu H}{k_B T}\right) f(\mu) d\mu + \chi_a H \quad (2)$$

where the Langevin function $L(x) = \coth(x) - 1/x$, being $x = \mu_0\mu H/kT$, is convoluted with a log-normal distribution of magnetic moments $f(\mu) = \exp[-(\ln(\mu/\mu_m)/2\sigma^2)]/\mu\sigma(2\pi)^{1/2}$, and χ_a is the high field susceptibility²⁷ related to surface magnetic disorder induced by the lack of symmetry. Not fully coordinated atoms at the surface of the particle lead to a magnetically frustrated layer which does not saturate even at 10 K and 2000 kA/m (see inset in Figure 7). The specific saturation magnetization is $M_s = N\langle\mu\rangle = N \int_0^\infty \mu f(\mu) d\mu$, where N is the particle number mass density and $\langle\mu\rangle$ the mean magnetic moment. χ_a values are of the order of $10^{-7} \text{ m}^3/\text{kg}$. Although the cycles are well fitted with eq 2 and the derived M_s values are correct, the so obtained mean magnetic moments display an unexpected temperature dependence.²⁸ In Figure 8 the mean values $\langle\mu\rangle = \mu_m \exp(\sigma^2/2)$ for various CS_i samples, obtained from best fits of M vs H data of dried colloid powders and frozen colloids, display an increasing behavior with temperature which is characteristic of ISP systems. Then, to determine the particle size distribution from the magnetic properties of each colloid and to compare it with the results obtained by TEM, $\langle\mu\rangle$ is derived from M vs H data acquired from colloidal samples at room temperature (see Figure 7) where the effect of the dipolar interaction on the recorded pattern is diminished. Using $\mu = M_s^{\text{bulk}}\rho V$ with magnetite density $\rho = 5175 \text{ kg/m}^3$ and $M_s^{\text{bulk}} = 86 \text{ Am}^2/\text{kg}$, a lognormal number distribution of magnetic core diameters $f(d_m)$ (with median $d_0 = (6\mu_0/\pi M_s^{\text{bulk}}\rho)^{1/3}$ and $\sigma_{d_m} = \sigma/3$ for spherical particles) is derived from $f(\mu)$ (see Figure 9). From mean $\langle d_m \rangle$, mean nanoparticle size is derived as $d = \langle d_m \rangle + \delta$ with $\delta = \langle d_m \rangle ((M_s^{\text{bulk}}/M_s)^{1/3} - 1)$, twice the magnetically frustrated surface layer thickness. From this analysis, it is concluded that

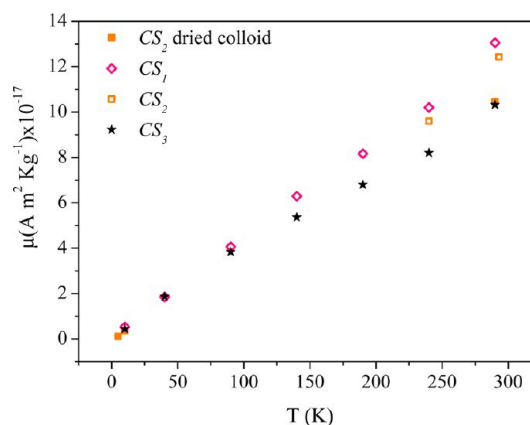


Figure 8. Mean magnetic moment derived from best fits of specific magnetization vs applied field using eq 2, for various frozen colloids, colloids (290 K), and CS_2 dried powder.

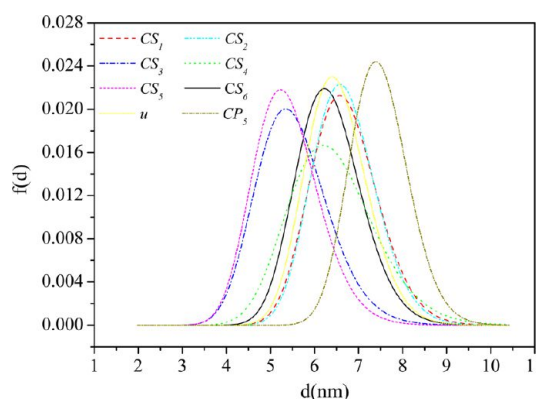


Figure 9. Log norm distribution of magnetic core diameters retrieved from the log norm magnetic moment distribution that fits the data in Figure 7.

the colloids CS_i and CP_i under study here are single domain and behave as interacting superparamagnets. For CS_1 , CS_2 , and CS_6 samples the size derived from magnetic cycles is larger than the mean sizes derived by TEM, while for CS_3 , CS_4 , and CS_5 the agreement is good. This discrepancy can be ascribed to the fact that TEM, although being a more direct determination, involves a smaller number of particles than the macroscopic magnetic measurement.

A charged particle moving in a solvent drags with it a layer of fluid molecules and counterions, resulting in an entity with a quite large hydrodynamic diameter d_H . In effect, in this study it was found that d_H values are 1 order of magnitude larger than the overall nanoparticle size including CA coating (see Table 1).

3.3. Specific Absorption Rates (SARs). The heating ability of the various colloids analyzed here was calorimetrically determined, and typical heating curves are shown in Figure 10. The time required to reach a given temperature, at fixed frequency, decreases with increasing field amplitude. SAR represents the power released per gram of magnetite upon ac-field application and is mainly given by the magnetization loop area. SAR values listed in Tables 1 and 2 were obtained from the initial slope of the heating curves using eq 1. These values range from 5.2 to 41.5 W/g for CS_i colloids, from 29 to 104 W/g for CP_i , and 203 W/g for the u -MNP colloid. The inspection of Figure 9 shows that for our samples there is no clear relation

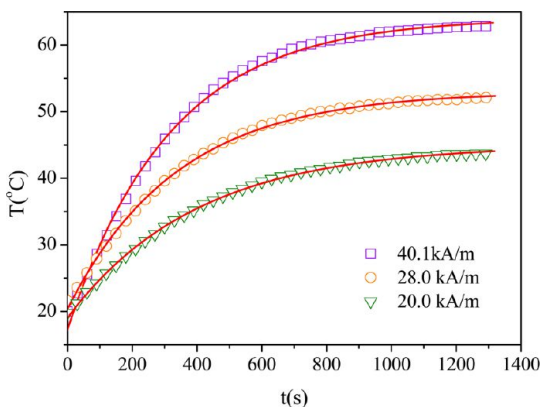


Figure 10. Heating curves acquired at 265 kHz and at various field amplitudes H_0 .

Table 2. Magnetic Characterization and Radiofrequency Dissipation of Magnetite Stable Aqueous Colloids and Uncoated Colloid^a

colloid	u	CP ₄	CP ₅	CP ₆
SAR (W/g)	203	28.78	93.6	104.2
M_s (Am ² /kg)	67.1	33.6	56.1	70.6
d_m (nm)	6.8	7.9	7.7	8.4
δ (nm)	0.6	3.2	1.2	0.6
[X]	8.28	6.1	10.2	6.0

^aCP_{*i*} (*i* = 4, 5, and 6) colloids synthesized as detailed in Table 1 and magnetically separated and u labels uncoated colloid. SAR stands for specific absorption rate at 40.1 kA/m and 265 kHz in Watts per gram of magnetite. Data derived from SQUID-DC magnetometry: M_s stands for specific saturation magnetization, d_m for magnetic core diameter, and δ for twice the magnetically frustrated layer thickness.

between SAR values either with magnetic core sizes or with distribution standard deviation σ_{dm} . For instance, CS₆, CS₄, and u colloid dissipate 5.2, 41.5, and 203 W/g, respectively, and all have nearly the same mean size. The main differences between these samples reside on saturation magnetization and blocking temperatures. Lower saturation magnetizations are assigned to larger magnetically frustrated layers and larger blocking temperatures to interaction and aggregation.

Now we evaluate SAR data in terms of the colloids' physical characterization given by M_s , $\langle d_m \rangle$, δ , T_{B0} , and d_H parameters listed in Tables 1 and 2.

Through the linear response theory the SAR parameter is theoretically given by¹⁹

$$\text{SAR} = \frac{\pi\mu_0 H_0^2 f}{\rho} \int_0^\infty \chi''(\tau(d)) f(d) dd \quad (3)$$

where μ_0 is the permeability of free space ($4\pi \times 10^{-7}$ H/m); $f(d)$ is the size distribution of MNPs having diameters d ; and χ'' is the out-of-phase magnetic susceptibility. SAR field amplitude dependence, plotted in Figure 11, displays an increasing behavior as expected from eq 3. The dependence departs from the linear relation expected for SAR plotted against H_0^2 for H_0 values larger than a maximum field. Once this field is exceeded, the area of the hysteresis loop does not change, and SAR remains constant.

For noninteracting nanoparticles, χ'' is a function of the relaxation time (τ) as $\chi''(\omega) = \chi_0((\omega\tau)/(1 + (\omega\tau)^2))$, with $\omega = 2\pi f$ and the dc-susceptibility $\chi_0 \cong (\mu_0 \rho^2 M_s^2 V)/(3k_B T)$, for small magnetic field amplitude. Because the colloids behave as

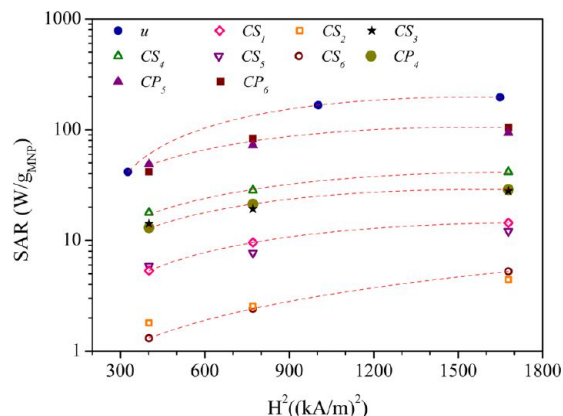


Figure 11. Specific absorption rate (SAR) field amplitude dependence. Dotted lines stand for second-order polynomial fits.

interacting superparamagnets, the dynamics of such systems strongly depends on many physical parameters related with the MNP properties and on the coupling strength. Whether the relaxation is driven by Brown ($\tau_B = (3\eta V_H)/(k_B T)$) or by Néel (τ_N) mechanisms depends on liquid carrier viscosity η , hydrodynamic particle volume (V_H), magnetic energy barrier E_a , and attempt time τ_0 , both E_a and τ_0 being size dependent.²⁹ The processes take place in parallel ($\tau^{-1} = \tau_B^{-1} + \tau_N^{-1}$) and prevails the one having the shorter relaxation time.

τ_B values calculated at 300 K using data listed in Table 1 and $\eta = 8.90 \times 10^{-4}$ Pa s for water fall in the range 0.2×10^{-5} to 0.9×10^{-5} s and are plotted vs SAR in Figure 12.

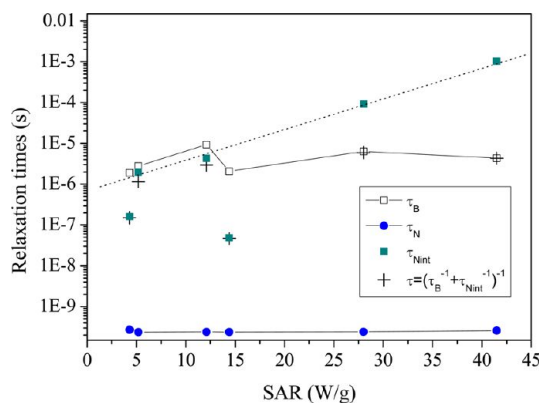


Figure 12. Brown relaxation times $\tau_B = (3\eta V_H)/(k_B T)$ calculated with $k_B = 1.38 \times 10^{-23}$ J K⁻¹, viscosity $\eta = 8.90 \times 10^{-4}$ Pa s, and $T = 300$ K. Néel relaxation times $\tau_N = \tau_0 \exp(k_{\text{eff}} V/k_B T)$ of isolated nanoparticles calculated using size-dependent anisotropy energy density $k_{\text{eff}}(d)$ and $\tau_0(d)$ interpolated from data in refs 31 and 32. Relaxation times τ_{Nint} for the Néel mechanism taking into account size dependence and interaction.

τ_N for isolating particles is given by³⁰ by

$$\tau_N = \tau_0 \exp(\sigma) \quad \text{with} \quad \sigma_a = E_a/k_B T \quad (4)$$

The energy E_a of isolated particles is equal to the magnetic anisotropy energy $K_{\text{eff}} V$, and K_{eff} is the size-dependent effective anisotropy energy density. For spherical particles, assuming that the overall anisotropy of the particle is uniaxial, the relation $K_{\text{eff}}(d) = K_{\text{bulk}} + (6/d)K_s$ is commonly used, where $K_{\text{bulk}} = 1 \times 10^4$ J/m³ is the bulk anisotropy energy density of magnetite at room temperature and K_s is the surface anisotropy density. This

$K_{\text{eff}}(d)$ relation models the increase of the anisotropy energy density with decreasing particle size and has been tested by Gilmore et al.³¹ in magnetite particles grown inside three protein cages of distinct size, where the cage served to constrain particle size and shape and to mute interparticle interaction. Using this relation with $K_s(d) = 2 \tanh(d/4)$, as in ref 31, we have retrieved K_{eff} for each particle size listed in Table 1. The corresponding τ_0 values were interpolated from the $\tau_0(d)$ relation built from data in refs 31 and 32. Evaluation of τ_N disregarding interactions results in values in the range $0.1\text{--}0.6 \times 10^{-9}$ s.

To take into account that the magnetic moments of interacting particles fluctuate with different relaxation times than those of isolated ones, a total energy barrier given by $E_a = K_{\text{eff}}V + E_{\text{int}}$ was assumed.³³ The interaction energy E_{int} was deduced from the shift of the ZFC maximum (Figure 6), disregarding τ_0 dependence with interactions, with respect to a noninteracting ensemble as $E_{\text{int}} = k_B(T_{\text{Bint}} - T_B)\ln(t_m/\tau_0)$. Here T_B is the blocking temperature expected for noninteracting particles of sizes listed in Table 1, as derived from the K_{eff} and τ_0 values mentioned above; T_{Bint} is the blocking temperature resulting from ZFC measurements (see Table 1); and $t_m \sim 100$ s is the SQUID measuring time. Then, Néel relaxation time for interacting particles τ_{Nint} was obtained with eq 4 with $\sigma = (K_{\text{eff}}V + E_{\text{int}})$. The results are shown in Figure 12 where the relaxation times are plotted vs SAR values determined with $H_0 = 40.1$ kA/m, i.e., maximum used H_0 value, larger than the anisotropy field. Interaction results in slower magnetic relaxation. A crossover between τ_{Nint} and τ_B behavior appears at 12.8 W/g. The larger SAR values come out with the more interacting colloids, i.e., for the particles displaying larger T_{Bi} (large E_{int} values). In those cases the process seems to be driven by a Brown mechanism, while for the other cases the Néel mechanism prevails.

The uncoated magnetite results in a very unstable suspension but produces the largest SAR of 200 W/g. Although particle size is similar to those of coated particles, the hydrodynamic size is $1.5 \mu\text{m}$ (polydispersity index $\sigma_{\text{PI}} = 0.5$) indicating the presence of large clusters of particles moving in the fluid. Blocking temperature is around 300 K, due to strong interactions. The analysis outlined above for coated colloids, when applied to the uncoated colloid, results in relaxation times various orders of magnitude larger. Still $\tau_B < \tau_{\text{Nint}}$, supporting the idea that interactions play an important role in magnetic fluid hyperthermia increasing nanoparticle energy dissipation.

SAR values against M_s are plotted in Figure 13 for all CP_i , CS_i , and u colloids. An increasing behavior is observed, as

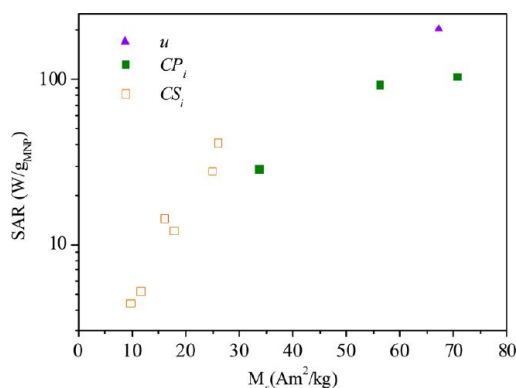


Figure 13. SAR dependence with specific saturation magnetization.

expected from the χ_0 dependence with M_s irrespective of nanoparticle size and dispersion. Lowering of M_s is assigned to a larger magnetically frustrated layer. Those CS_i colloids of MNP coated at lower pH_{ads} and displaying larger electrostatic stability present lower M_s values. The corresponding CP_i colloids display larger M_s and SAR values consistently with the idea of MNPs having less coating material on their surfaces and being more effectively attracted to the magnet. These observations suggest that citric acid may have an influence on the surface of the MNP, producing larger frustrated layers which on one side improve nanoparticle suspension stability but on the other one lower SAR values. The optimum synthesis condition to accomplish both properties, extremely high stability in suspension at neutral pH and large SAR values, is obtained by citric acid coating at $\text{pH}_{\text{ads}} = 6.25$.

3.4. In Vitro Biocompatibility of CA-Coated MNPs Internalized in A549 Cells. The materials involved in the synthesis procedure (water, CA, and magnetite) are known to display good biocompatibility. However, since interfacial processes may take place when MNPs are dispersed in biological media changing their surface reactivity and consequently their toxicity,³⁴ we have tested the viability of our nanoparticles in A549 cells. Figure 14 shows the cytometric analysis of double-labeling for Annexin V and PI assay for the A549 cell without MNP exposure and internalized with three distinct CS_4 colloid concentrations. Viable cells are negative for both labelers (DL quadrant); apoptotic cells are PI negative and annexinV positive (DR quadrant); while necrotic cells are positive for both (UR quadrant). After internalization with CS_4 colloids at concentrations of 34, 67, and 135 $\mu\text{g}_{\text{Fe}_3\text{O}_4}/\text{mL}$, the percentages of viable cells are 94.7%, 95.1%, and 81.3%, respectively. Only for the highest concentration, viability decrease compared with 84.7% of control cells is observed. The fact that the control culture shows a lower viability than the lower concentrated cultures may be due to an overgrown control culture. It is concluded that 12 h exposure to CA-coated Fe_3O_4 nanoparticles at low concentration is not altering A549 cell viability. Then, citric acid coated magnetite aqueous suspensions at neutral pH were internalized without causing cell toxicity.

CONCLUSIONS

We have presented a detailed and extensive study of synthesis conditions, magnetic properties, and radiofrequency dissipation efficiency of various biocompatible citric acid coated magnetite aqueous suspensions at neutral pH. The preparation method enables us to control the long-term stability of the suspension varying the citric acid adsorption pH. The largest stability at neutral medium is achieved for the nanoparticles coated at pH of 4.58, where citric acid mainly binds to the particle surface by one carboxylate, leaving two free and charged dangling ends. Citric acid influences the surface of the MNP, producing thick magnetically frustrated layers which on one side improve nanoparticle suspension stability but on the other one reduce SAR values. Finally, our results indicate that dipolar interactions between the nanoparticles play a key role in the Néel relaxation mechanism and dissipation efficiency. Magnetic relaxation becomes slower for interacting colloids, and heating efficiency increases. The largest SAR values arise from the more interacting nanoparticles, a case where Néel relaxation times become larger than Brown relaxation times, leading the Brown dissipation mechanism to prevail. It is shown that SAR data cannot be easily reproduced using the magnetic data and the

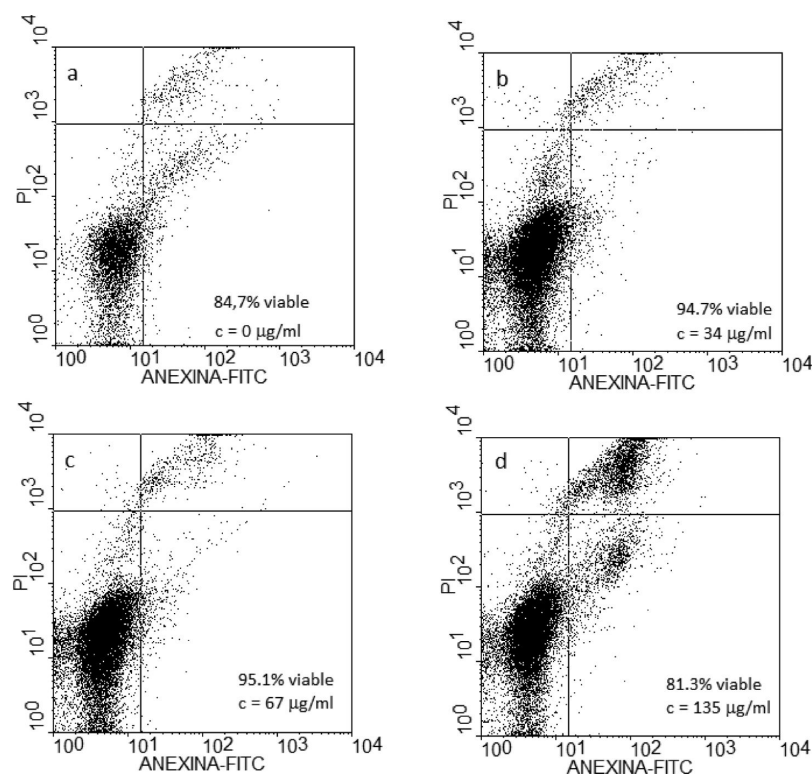


Figure 14. Dot plot obtained from Flow Cytometry data (Annexin/PI staining) of A549 cells. For all plots, Down Left (DL), Down Right (DR), and Up Right (UR) quadrants correspond to viable, apoptotic, and necrotic cells, respectively. Control (a), after 12 h internalization at 34 $\mu\text{g/mL}$ (b), 67 $\mu\text{g/mL}$ (c), and 135 $\mu\text{g/mL}$ (d).

most currently used theoretical expressions, due to the presence of dipolar interactions between the nanoparticles. Interaction energy was included in the theoretical expressions through the quantity $\sigma = (K_{\text{eff}}V + E_{\text{int}})/k_{\text{B}}T$ and its value inferred from the blocking temperature shift.

■ ASSOCIATED CONTENT

● Supporting Information

Figure S1. This material is available free of charge via the Internet at <http://pubs.acs.org>.

■ AUTHOR INFORMATION

Corresponding Author

*E-mail: raap@fisica.unlp.edu.ar.

Notes

The authors declare no competing financial interest.

■ ACKNOWLEDGMENTS

This work has been funded by CONICET (PIP 01111), ANPCyT (PICT 00898), and UNLP-X11/556 of Argentina. Z-potential measurements were performed at INQUISUR, UNS-CONICET, by V. Lassalle whose help is deeply acknowledged. DC magnetometry was performed using SQUID equipment of Red de Magnetismo y Materiales Magnéticos (RN3M) and VSM equipment of IFLP-CONICET. We thank FAPESP and C2NANO - Center for Nanoscience and Nanotechnology/MCT (# 13872) for the use of TEM equipment. We greatly appreciate the help from R. Dewey and A. Carrea of IIB-INTECH (UNSAM) with the flow cytometry analysis and Y. Sosa and R. Goya for help with cell culture experiments, carried out at INBIOLP - Patología B - CONICET. Marcela B. Fernández van Raap, Patricia Rivas, Pedro Mendoza Zélis,

Gustavo A. Pasquevich, and Francisco H. Sánchez are members of IFLP- CONICET; José L. Alessandrini is a member of Departamento de Física de la UNLP; and M. Elisa de Sousa and Pablo Girardin are fellows of FONCYT and CONICET, Argentina.

■ ABBREVIATIONS

AS, ammonia solution; CA, citric acid; CP_i, ith pellet colloid; CS_i, ith supernatant colloid; DTA, differential thermal analysis; DLS, dynamic light scattering; d_{H} , hydrodynamic diameter; DMEM, Dulbecco's modified eagle medium; FC, field cooling; IEP, isoelectric point; ISP, interacting superparamagnet; MNP, magnetic nanoparticles; PI, propidium iodide; pK_{a} , acid dissociation constant; u -MNP, uncoated magnetic nanoparticles; rf, radiofrequency; SAR, specific absorption rate; TEM, transmission electron microscopy; TG, thermogravimetry; XRD, X-ray diffraction; ZFC, zero field cooling; σ_{PL} , polydispersity index

■ REFERENCES

- (1) Rosensweig, R. *Ferrohydrodynamics*; Dover books on physics; Dover Publications: Mineloa, NY, 1997.
- (2) Weinstein, J. S.; Varallyay, C. G.; Dosa, E.; Gahramanov, S.; Hamilton, B.; Rooney, W. D.; Muldoon, L. L.; Neuwelt, E. A. *J. Cereb. Blood Flow Metab.* **2010**, *30* (1), 15–35.
- (3) Gupta, A. K.; Gupta, M. *Biomaterials* **2005**, *26*, 3995–4021.
- (4) Smirnov, P. *Methods Mol. Biol.* **2009**, *512* (II), 333–353.
- (5) Dobson, J. *Gene Ther.* **2006**, *13*, 283–287.
- (6) Chomoucka, J.; Drbohlavova, J.; Huska, D.; Adamc, V.; Kizek, R.; Hubalek, J. *Pharmacol. Res.* **2010**, *62*, 144–149.
- (7) Hilger, I.; Andrä, W.; Hergt, R.; Hiergeist, R.; Schubert, H.; Kaiser, W. A. *Radiology* **2001**, *218*, 570–575.

- (8) Silva, A. C.; Oliveira, T. R.; Mamani, J. B.; Malheiros, S. M. F.; Malavolta, L.; Pavon, L. F.; Sibov, T. T.; Amaro, E., Jr.; Tannús, A.; Vidoto, E. L. G.; et al. *Int. J. Nanomed.* **2011**, *6*, 591–603.
- (9) Gazeau, F.; Wilhelm, C. *Future Med. Chem.* **2010**, *2* (3), 397–408.
- (10) Batlle, X.; Pérez, N.; Guardia, P.; Iglesias, O.; Labarta, A.; Bartolomé, F.; García, L. M.; Bartolomé, J.; Roca, A. G.; Morales, M. P.; et al. *J. Appl. Phys.* **2011**, *109*, 1–6.
- (11) Wei, W.; Quanguo, H.; Changzhong, J. *Nanoscale Res. Lett.* **2008**, *3*, 397–415.
- (12) Viota, J. L.; Arroyo, F. J.; Delgado, A. V.; Horno, J. J. *Colloid Interface Sci.* **2010**, *344* (1), 144–149.
- (13) Kogan, M. J.; Olmedo, M. J. I.; Hosta, L.; Guerrero, A. R.; Cruz, L. J.; Albericio, F. *Nanomedicine* **2007**, *2* (3), 287–306.
- (14) Campelj, S.; Makovec, D.; Drofenik, M. *J. Phys.: Condens. Matter* **2008**, *20*, 204101/1–204101/5.
- (15) Răcuciu, M. *Curr. Appl. Phys.* **2009**, *9* (5), 1062–1066.
- (16) Nigama, S.; Barick, K. C.; Bahadur, D. *J. Magn. Magn. Mater* **2011**, *323*, 237–243.
- (17) Yallapua, M. M.; Othmanb, S. F.; Curtisb, E. T.; Guptaa, B. K.; Jaggia, M.; Chauhana, S. C. *Biomaterials* **2011**, *32*, 1890–1905.
- (18) Sahoo, Y.; Goodarzi, A.; Swihart, M. T.; Ohulchansky, T. Y.; Kaur, N.; Furlani, E. P.; Prasad, P. N. *J. Phys. Chem. B* **2005**, *109*, 3879–3885.
- (19) Rosensweig, R. E. *J. Magn. Magn. Mater.* **2002**, *252*, 370–374.
- (20) Massart, R. *IEEE Trans. Magn.* **1981**, *MAG-17* (2), 1247–1248.
- (21) Lefebure, S.; Dubois, E.; Cabuil, V.; Neveu, S.; Massart, R. *J. Mater. Res.* **1998**, *13* (10), 2975–2981.
- (22) Sun, Z.; Su, F.; Forsling, W.; Samskog, P. *J. Colloids Interface Sci.* **1998**, *197* (1), 151–159.
- (23) Provencher, S. W. *Comput. Phys. Commun.* **1982**, *27*, 213–227.
- (24) van Engeland, M.; Nieland, L. J. W.; Ramaekers, F. C.S.; Schutte, B.; Reutelingsperger, C. P. M. *Cytometry* **1998**, *31*, 1–9.
- (25) Shen, L.; Laibinis, P. E.; Hatton, T. A. *Langmuir* **1999**, *15*, 447–453.
- (26) Pnias, D.; Taxiarchou, M.; Paspaliaris, I.; Kontopoulos, A. *Hydrometallurgy* **1996**, *42* (2), 257–265.
- (27) Dutta, P.; Manivannan, A.; Seehra, M. S. *Phys. Rev. B* **2004**, *70* (174428), 1–7.
- (28) Allia, P.; Coisson, M.; Tiberto, P.; Vinai, F.; Knobel, M.; Novak, M. A.; Nunes, W. C. *Phys. Rev. B* **2001**, *64* (14), 1–12.
- (29) Dormann, J. L.; Fiorani, D.; Tronc, E. *Magnetic Relaxation in Fine-Particle Systems*, Advances in Chemical Physics 98; Wiley: New York, 2007.
- (30) Raikher, Y. L.; Shliomis, M. I. *The effective field method in the orientational kinetics of magnetic fluids and liquid crystals*, Advances in Chemical Physics 87; Wiley: New York, 1994; Chapter 8, p 595.
- (31) Gilmore, K.; Idzerda, Y. U.; Klem, M. T.; Allen, M.; Douglas, T.; Young, M. *J. Appl. Phys.* **2005**, *97*, 10B301/1–10B301/3.
- (32) Fannin, P. C.; Marin, C. N.; Raj, K.; Couper, C.; Barvinschi, P. *J. Magn. Magn. Mater* **2012**, *324*, 3443–3447.
- (33) Dormann, J. L.; Bessays, L.; Fiorani, D. *Solid State Phys. C* **1988**, *21*, 2015–2034.
- (34) Casals, E.; Gonzalez, E.; Puentes, V. F. *J. Phys. D: Appl. Phys.* **2012**, *45*, 443001/1–443001/15.